CREEP CRACK GROWTH PREDICTIONS IN INCO 718 USING A CONTINUUM DAMAGE MODEL

Kevin P. Walker
Engineering Science Software, Inc.
Smithfield, Rhode Island 02906

Dale A. Wilson
Pratt and Whitney Aircraft
Government Products Division
East Hartford, Connecticut 06108

Creep crack growth tests have been carried out in compact type specimens of INCO 718 at 1200°F (649°C). Theoretical creep crack growth predictions have been carried out by incorporating a unified viscoplastic constitutive model and a continuum damage model into the ABAQUS nonlinear finite element program.

Material constants for both the viscoplastic model and the creep continuum damage model were determined from tests carried out on uniaxial bar specimens of INCO 718 at 1200°F (649°C).

A comparison of the theoretical creep crack growth rates obtained from the finite element predictions with the experimentally observed creep crack growth rates indicates that the viscoplastic/continuum damage model can be used to successfully predict creep crack growth in compact type specimens using material constants obtained from uniaxial bar specimens of INCO 718 at 1200°F (649°C).

INTRODUCTION

The Air Force and Pratt and Whitney Aircraft are developing technology to allow for an eventual damage tolerant design approach to turbine engine components and to retire existing components based on the detection of service initiated flaws. This approach is based heavily on the capability to predict the growth of flaws in critical structural components during the service life of the component. The majority of critical structural components operate at elevated temperatures where plasticity and time-dependent creep occur, particularly in regions of stress concentration and near the tips of fatigue cracks. Considerable research is currently being conducted on modeling crack growth behavior in engine materials. These research efforts require an understanding of crack tip behaviour in order to successfully evolve realistic crack growth criteria. Because of the complex inelastic behaviour, closed-form solutions to crack problems are not practical. An alternative approach is to use finite element methods for modeling test geometries. Such an approach, however, depends heavily on realistic constitutive models of the material behaviour as well as localized failure criteria for crack growth problems.

This paper presents some results on creep crack growth obtained under a contract [1] with the Air Force Materials Laboratory at Wright Patterson Air Force Base under the cognizance of Dr. Ted Nicholas. The Program involved the development of a constitutive model for INCO 718, a nickel-base alloy, at 1200°F (649°C) under monotonic, cyclic, and sustained loading. This model has the capability of accounting for load history effects as well as material failure or damage accumulation. The model has been incorporated into a nonlinear finite element program to simulate the crack growth behaviour in laboratory test specimens, and data have been generated to evaulate the applicability of the model. Development of the model was based on prior constitutive modeling efforts, and as such, primarily involved modifications and refinements to established approaches.

PROBLEM DESCRIPTION AND SOLUTION

At elevated temperatures the material in the vicinity of a crack tip can fail or rupture under creep (constant load) conditions due to the high stress concentration. To predict creep crack growth analytically it is first necessary to determine the stress-strain behaviour of the material in the vicinity of the crack tip. Once the stress and strain histories are known at a particular point, the time required to fail or rupture the material at that point can then be determined by a suitable failure criterion.

The theoretical effort makes use of a unified viscoplastic constitutive formulation to determine the time-dependent material behaviour in the crack tip vicinity, while a continuum damage model

is used to predict the time required to fail a particular point in the crack tip neighborhood. Both the viscoplastic constitutive model and the continuum damage model have been incorporated as a FORTRAN subroutine into the ABAQUS [2] general purpose nonlinear finite element program. When the continuum damage criterion dictates that the material at the Gaussian integration point in the finite element closest to the crack tip has failed, the node at the crack tip is released, and the crack advances to the adjacent node in the crack plane.

Under creep conditions the small amount of crack growth is difficult to determine by conventional experimental crack measuring techniques. Instead of measuring crack length as a function of time, the displacement of two points located on either side of the crack tip is monitored as a function of time by an optical interferometric displacement measurement technique. The nodes along the crack plane in the finite element model are released in such a manner that the computed displacements of the two points, due to both the viscoplastic material behaviour and the crack growth, matches the experimental displacements as time progresses. Crack length, as a function of time, then becomes a product of the finite element analysis rather than an input. Since the failure criterion under creep conditions is determined by a continuum damage model, the material constants in this model can be chosen to give a least square fit to the creep crack growth experiments in the INCO 718 compact type specimens at 1200°F (649°C) carried out under different applied loads. The material constants in the continuum damage model can also be determined to give a least square fit to the creep rupture data obtained from uncracked uniaxial specimens of INCO 718 at 1200°F (649°C). If creep crack growth is governed by creep rupture of the material directly ahead of the crack tip, then the material constants determined from the creep rupture experiments on the uncracked uniaxial specimens should coincide with those obtained from the creep crack growth experiments on the compact type specimens.

The use of combined experimental and theoretical procedures to determine crack growth criteria has been labeled the Hybrid Experimental-Numerical procedure by Kobayashi [3]. Hinnerichs and his colleagues [4] used this procedure to determine a creep crack growth criterion for IN 100 at 1350°F (732°C) from experiments carried out on a centre-cracked plate test specimen by Sharpe [5]. They found that a critical damage accumulation criterion for creep crack growth similar to that employed in the present work gave good correlation with the experiments conducted by Sharpe.

CONSTITUTIVE FORMULATION

Cyclic hysteresis loops and creep curves were generated for INCO 718 at 1200°F (649°C). Figure 1 shows a logarithmic plot of stress vs. inelastic strain rate from creep tests and cyclic hysteresis loops generated in the present work and from tests conducted by Domas, Sharpe, Ward, and Yau [6]. The plot shows the variation of secondary creep rate (or extension rate in a uniaxial hysteresis test) with applied stress. Discrepancies between the present data

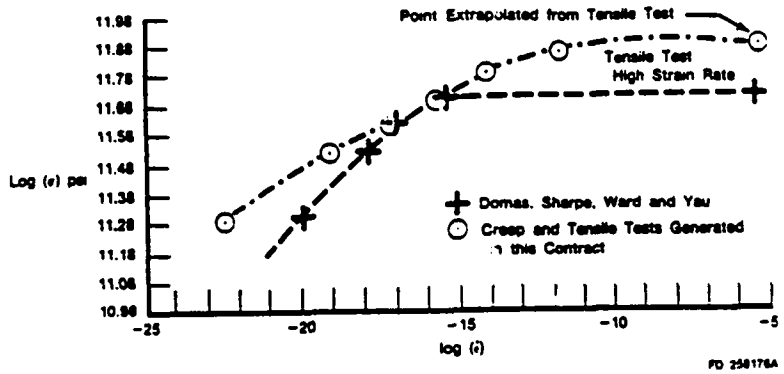

Figure 1. - Plot of Log (Stress) vs Log (Plastic Strain Rate) from Creep and Tensile Tests on INCO 718 at 649 °C.

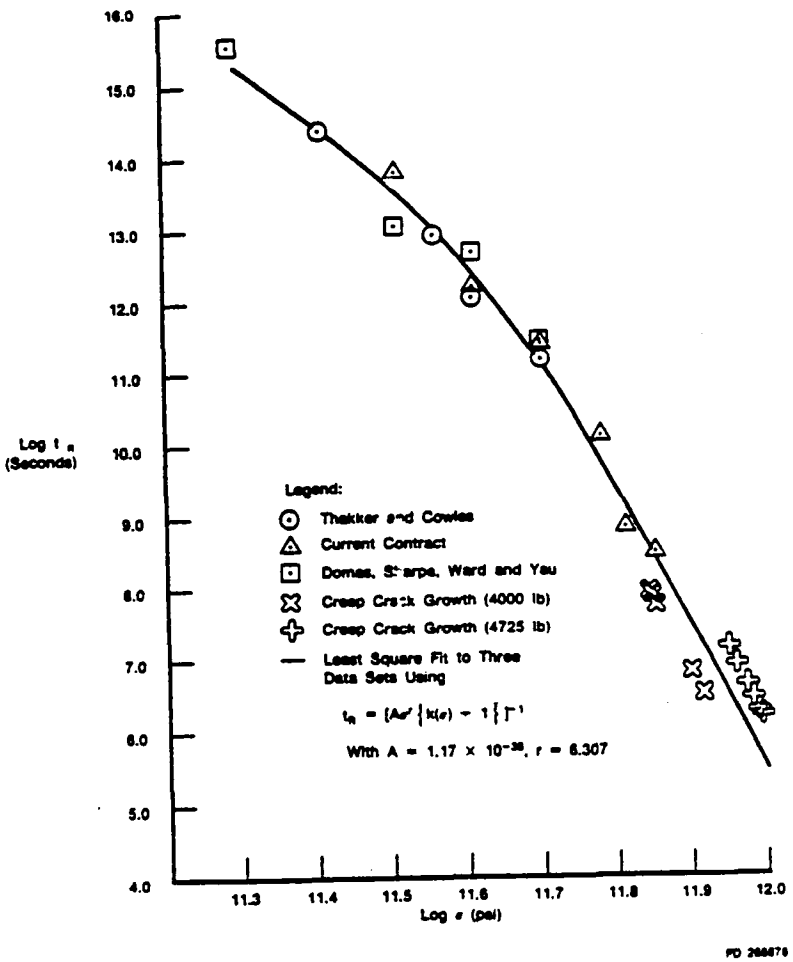

Figure 2. - Experimental Creep Rupture Data and Least Square Theoretical Fit

and that generated by Domas, et al [6], occur at both low and high stress levels. At high stress levels corresponding to the uniaxial hysteresis tests, the data points are estimates obtained by extrapolating the test data to obtain the ultimate stress values.

At high strain rates (in this context 10^{-4} to 10^{-3} per second) the material behaviour becomes insensitive to strain rate. This may be observed in the flattening of the logarithmic stress vs. inelastic strain rate curves shown in Figure 1, and is exhibited by the present data and by the data generated by Sharpe and his colleagues.

A power law expression [7] for the inelastic strain rate in terms of the applied stress and equilibrium stress was first fitted to the creep and hysteresis data. When fitting unified viscoplastic models to test data, the usual procedure is to assume that the functional form of the inelastic strain rate expression is correct, and that any deviation of the test data from the assumed functional form is due to thermal recovery of the state variables. In this manner the material constants for both rate effects and thermal recovery can be determined from the test data. A reasonable correlation of stress vs. strain rate was achieved with the power law at low to intermediate strain rates provided thermal recovery was taken into account. However, the power law may be expected to hold only over a relatively small strain rate range, and the stresses at high strain rates tend to be overestimated with a power law expression. This was clearly evident in the predicted stress results for strain rates of 5.3×10^{-4} per second and 5.3×10^{-3} per second used in the hysteresis loop testing. To obtain a better overall correlation of stress vs. strain rate, it was decided to use an exponential law for the inelastic strain rate in place of the power law. This provided a much better fit to the experimental data at all strain rates without including thermal recovery effects. Thermal recovery is present at 1200°F (649°C), but derive the current set of material constants, thermal recovery has been neglected. Table 1 shows the correlation between experiment and theory using the exponential constitutive formulation given in Appendix 1.

Table 1 *Stress vs Strain Rate With Exponential Law*

$\dot{\varepsilon}$ (Per Second)	σ (psi, Test)	σ (psi, Theory)
5.3 E-3	172000 (Extrapolated)	177536
5.3 E-4	—	164492
6.88 E-6	140000	140000
8.22 E-7	130000	127971
1.52 E-7	120000	118406
3.66 E-8	110000	110435
5.67 E-9	100000	100000
3.65 E-10	80000	86377

Table 2 *Creep Rupture Details of INCO 718 at 1200°F (649°C) Obtained in Present Contract*

Stress (ksi)	Strain on Loading: Elastic (%)	Strain on Loading: Inelastic (%)	Rupture Time (hr)	Final Elongation (%)	Reduction in Area (%)
140	0.506	0.639	1.4	8.2	12.6
135	0.610	0.607	2.0	9.0	14.2
130	0.251	0.151	6.9	7.4	12.2
120	0.279	0.056	25.5	10.5	16.2
110	0.292	0.006	56.7	8.0	13.2
100	0.286	0.0	281.1	13.4	41.9
80	0.277	0.0	Discontinued after 358 hr		

Table 3 *Creep Rupture Details of INCO 718 at 1200°F (649°C) Obtained by Domas, Sharpe, Ward, and Yau [5]*

Stress (ksi)	Rupture Time (hr)	Average Standard* Rupture Time (hr)
120	26	15
110	92	50
100	131	160
80	1583	1600

*C50TF6 Specification

Table 4 *Creep Rupture Details of INCO 718 at 1200°F (649°C) Obtained by Thakker and Cowles [8]*

Stress (ksi)	Strain on Loading: Elastic (%)	Strain on Loading: Inelastic (%)	Rupture Time (hr)	Final Elongation (%)	Reduction in Area (%)
120	0.597	0.060	20.1	12.1	15.9
110	0.581	0.012	48.3	14.8	52.3
105	0.476	0.009	116.0	23.7	56.8
90	0.450	0.005	494.8	28.0	61.3

Table 5 *Comparison of Theoretical and Experimental Creep Rupture Times*

Stress (psi)	Rupture Time Experiment (sec)	Rupture Time (sec) from $t_R=[A\,\sigma^r\,\{k(\sigma)+1\}]^{-1}$
140000	5040	5041
130000	24840	21000
120000	91800	85015
110000	204120	315123
100000	1011960	1011687

$A = 2.394 \times 10^{-43}$, $r = 7.22$, $k(\sigma) = 1 + 1.011E\text{-}4e^{9.446E\text{-}5\,\sigma}$

INCO 718 displays cyclic softening at 1200°F (649°C). The softening is observed in the decrease in the stress amplitude of the hysteresis loops as cycling proceeds under constant strain amplitude. It can also be observed in the increase in the width of the hysteresis loops under constant stress amplitude in fatigue testing. This cyclic softening can be modeled with the viscoplastic formulation at small cyclic strain amplitudes by allowing the drag stress state variable to decrease with cumulative inelastic strain. In the finite element creep crack growth calculations the drag stress was assumed to be constant and cyclic softening was not permitted. Material constants for the cyclic softening case and for the noncyclic softening case used in the finite element calculations are listed in Appendix 1.

Tertiary creep and creep damage accumulation have been included in the constitutive formulation by using Chaboche's continuum creep damage model [8]. Details of this model are given in Appendix 2. Experimental results of creep rupture time and creep rupture strain as a function of stress level are given in Tables 2, 3 and 4. A comparison of theoretical and experimental creep rupture times is given in Table 5.

Material constants for the creep damage model were determined from creep rupture tests on uniaxial bar specimens of INCO 718 at 1200°F (649°C). The specimens were given a standard heat treatment per specification AMS 5596C as follows:

Solution anneal at 1750°F (854°C) for one hour. Air cool to below 932°F (500°C). Age at 1325°F (718°C) for eight hours. Furnace cool to 1150°F (621°C). Age at 1150°F (621°C) for a total time of eighteen hours aging, cooling, and aging. Air cool to room temperature. The test material was furnished in the form of 0.5 in. (12.7mm.) thick flat plates having nominal dimensions 12x4 in. (305x102mm).

Figure 2 shows a logarithmic plot of stress vs. rupture time for the creep rupture tests performed in the current work and for creep rupture data generated by Domas et al [6] and by Thakker and Cowles [9]. The rupture time corresponding to an initial tensile stress level can be determined from the uniaxial form of the damage growth relation presented in Appendix 2. This relationship may be written in the uniaxial form

$$\frac{dD}{dt} = \frac{A\sigma^r}{(1-D)^{k(\sigma)}}. \qquad (1)$$

Integration between the limit D=0 to D=1 gives the creep rupture time in the form

$$t_R = [A\sigma^r\{k(\sigma) + 1\}]^{-1}. \qquad (2)$$

A least squares fit to the three data sets is achieved with the values

$$A=1.17\times10^{-38}, r=6.31, k(\sigma)=1+(1.011\times10^{-4})\exp(9.446\times10^{-5}\sigma).$$

This fit is shown as the solid line in Figure 2. For the data generated in the current work a least square fit is achieved with the values

$$A=2.394\times10^{-43}, r=7.22, k(\sigma)=1+(1.011\times10^{-4})\exp(9.446\times10^{-5}\sigma).$$

FINITE ELEMENT MODELING

The unified viscoplastic constitutive formulation including Chaboche's continuum creep damage model outlined in the appendices was incorporated into a FORTRAN subroutine of the ABAQUS general purpose nonlinear finite element program. The ABAQUS program solves the nonlinear finite element equilibrium equations by a Newton-Raphson iterative method. For quasistatic loading conditions the finite element equilibrium equations are solved in the form:

$$\Sigma\left(\int_V B^T J B \, dV\right) c^k = P(t+\Delta t) - \Sigma\int_V B^T(\sigma(t) + \Delta\sigma(\Delta u^k))dV, \tag{3}$$

$$\Delta u^{k+1} = \Delta u^k + c^k. \tag{4}$$

In these equations the matrix B transforms incremental nodal displacements to incremental strains according to the relationship

$$\Delta\epsilon = B\,\Delta u. \tag{5}$$

The stress increment for the unified viscoplastic constitutive formulation is a function of the strain increment, and is therefore a function of the nodal displacement increments via equation (5). Equation (3) provides the correction to the kth iteration for the displacement increment.

In order to implement the Newton-Raphson iterative method for solving the finite element equilibrium equations, it is necessary to provide the Jacobian matrix J in equation (3). This matrix is determined from the relationship

$$J = \left(\frac{\partial\sigma}{\partial\epsilon}\right)_{t+\Delta t}. \tag{6}$$

Since the differential form of the unified viscoplastic formulation results in a mathematically stiff system of differential equations, the stress increment resulting from a given strain increment must be determined by a subincrement method. The simplest method, and the one used in the present work, is to split the finite element increment into a number of equally sized subincrements and to integrate the viscoplastic equations over each subincrement with an Euler forware difference method. This can result in an unstable integration operator if the subincrement size is too large. In the FORTRAN subroutine the inelastic strain rate is determined by the forward difference representation of equation (1) of Appendix 3. If the magni-

tude of the argument of the exponential factor in equation (1) exceeds the value of thirty (30) in any subincrement, the integration procedure is stopped. The number of subincrements is then tripled and the subincrement integration procedure is restarted from the beginning. This procedure is repeated until no subincrement produces an exponential argument greater in magnitude than thirty.

Since the Jacobian matrix J cannot be obtained in algebraic form when a subincremental procedure is used, it is necessary to obtain this matrix numerically. A numerical Jacobian matrix is computed in the following manner. First the viscoplastic constitutive subroutine is entered to determine the stress increments $\Delta\sigma_{xx}$, $\Delta\sigma_{yy}$, $\Delta\sigma_{xy}$ corresponding to the strain increments $\Delta\varepsilon_{xx}$, $\Delta\varepsilon_{yy}$, $\Delta\varepsilon_{xy}$. Let $\Delta\sigma^{xx}_{xx}$, $\Delta\sigma^{xx}_{yy}$, $\Delta\sigma^{xx}_{xy}$ be the stress increments corresponding to the perturbed strain increments $\Delta\varepsilon_{xx}+0.01\Delta\varepsilon_{xx}$, $\Delta\varepsilon_{yy}$, $\Delta\varepsilon_{xy}$; let $\Delta\sigma^{yy}_{xx}$, $\Delta\sigma^{yy}_{yy}$, $\Delta\sigma^{yy}_{xy}$ correspond to the perturbed strain increments $\Delta\varepsilon_{xx}$, $\Delta\varepsilon_{yy}+0.01\Delta\varepsilon_{yy}$, $\Delta\varepsilon_{xy}$; and let $\Delta\sigma^{xy}_{xx}$, $\Delta\sigma^{xy}_{yy}$, $\Delta\sigma^{xy}_{xy}$ correspond to the perturbed strain increments $\Delta\varepsilon_{xx}$, $\Delta\varepsilon_{yy}$, $\Delta\varepsilon_{xy}+0.01\Delta\varepsilon_{xy}$. The numerical plane stress Jacobian is then determined from the matrix relation:

$$J = \begin{bmatrix} \dfrac{\Delta\sigma^{xx}_{xx} - \Delta\sigma_{xx}}{0.01\Delta\epsilon_{xx}} & \dfrac{\Delta\sigma^{yy}_{xx} - \Delta\sigma_{xx}}{0.01\Delta\epsilon_{yy}} & \dfrac{\Delta\sigma^{xy}_{xx} - \Delta\sigma_{xx}}{2(0.01\Delta\epsilon_{xy})} \\ & \dfrac{\Delta\sigma^{yy}_{yy} - \Delta\sigma_{yy}}{0.01\,\Delta\epsilon_{yy}} & \dfrac{\Delta\sigma^{xy}_{yy} - \Delta\sigma_{yy}}{2(0.01\Delta\epsilon_{xy})} \\ \text{Symmetric} & & \dfrac{\Delta\sigma^{xy}_{xy} - \Delta\sigma_{xy}}{2(0.01\Delta\epsilon_{xy})} \end{bmatrix} \quad (7)$$

Thus, the plane stress Jacobian matrix requires four calls to the viscoplastic constitutive subroutine at each Gaussian integration point in the structural model. One call is required to obtain the unperturbed stress increment, whilst three additional calls are required for each perturbed strain increment.

It is necessary to use the same number of subincrements in each of the four calls to the viscoplastic constitutive subroutine. Otherwise, the Jacobian matrix will contain components of "noise" resulting from the operation $\partial\sigma/\partial$(change in number of subincrements). For this reason it was not considered worthwhile to change the size of the subincrements by means of some self-adaptive error detecting method during the finite element integration step, since the size of each subincrement would have to be stored in order to use the same subincrement breakup in each of the perturbed strain increment calls to the constitutive subroutine. The simple procedure of

using enough subincrements to prevent the magnitude of the exponential argument from exceeding the value of thirty was therefore adopted.

In order to determine the number of subincrements to be used in the finite element integration step, the following empirical procedure was adopted. Let e denote the largest absolute value of either the xx, yy or xy components of the finite element strain increment for the case of plane stress. Numerical studies have shown that the forward difference integration procedure is generally stable provided the strain increment does not exceed the value of 10^{-4}. The number of subincrements for a given Gaussian integration point in some finite element in the structure is then determined as $e/10^{-4}$. In crack propagation experiments in a superalloy compact type specimen, the stress and strain increments are large only in the immediate vicinity of the crack tip. All other elements away from the crack tip vicinity generally experience small strain increments. Thus, in the element ahead of the crack tip, the Gaussian integration points may require 50 subincrements, while those elements further from the crack tip generally require only 2 or 3 subincrements.

If the finite element load increment is large, then all of the finite elements will require a large number of subincrements to integrate the constitutive relations. This will be the case for structures which are free of large stress or strain gradients. However, for cracked structures, the large stress and strain gradients in the vicinity of the cracks and stress risers prevent large finite element load increments from being taken. This arises from the fact that the large stress or strain gradients give a very small radius of convergence to the Newton-Raphson iteration method for solving the finite element equilibrium equations. This small radius of convergence of the iteration method for cracked structures is not peculiar to the Newton-Raphson method. During the present work a Picard, or successive substitution method (as used in the MARC program), was also used to solve the finite element equilibrium equations. For cracked structures the radius of convergence of this iteration method was also found to be very small. In addition, the rate of convergence for small increments with the Picard method is linear, whereas the rate of convergence of the Newton-Raphson method is quadratic. For this reason the Newton-Raphson iteration method for solving the finite element equilibrium equations for cracked structures appears preferable to the Picard successive substitution procedure.

The fact that small finite element increments must be used to solve the equilibrium equations for cracked structures implies that most of the structure is subjected to very small finite element strain increments. One or two subincrements are then required for most of the Gaussian points in the structure, and it is doubtful if more refined integration methods (implicit) are required for these structures.

CREEP CRACK GROWTH MODELING

Experimental creep crack growth data have been generated by loading compact type specimens of INCO 718 with applied load levels of 4000 lb. and 4725 lb. at 1200°F (649°C). It is difficult to measure crack length as a function of time on the surface of the compact type specimen with any accuracy due to the fact that the amount of crack growth is usually very small, and the crack may grow internally in the specimen without associated surface crack growth. Instead of measuring creep crack growth directly, displacements across the crack were measured as a function of time at the two points shown in Figure 3 by means of speckle interferometry. Finite element calculations were then used to determine the theoretical creep crack growth rate with computed displacements at the two speckle interferometry points which agree with the experimental measurements. Crack growth versus time is then obtained indirectly from the analytical results in the manner employed by Hinnerichs et al [4].

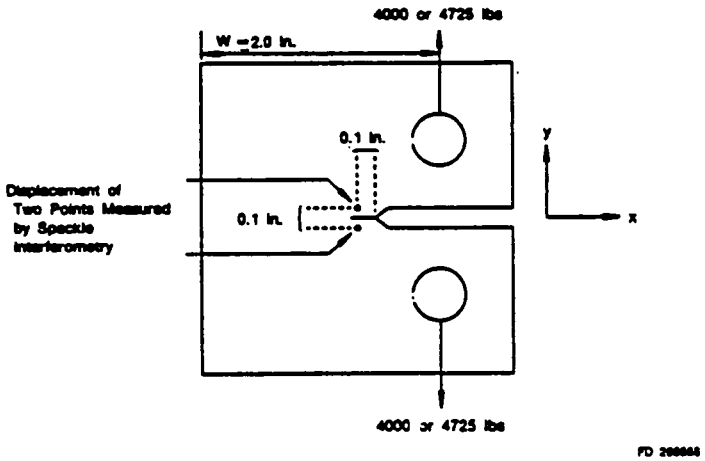

Figure 3. - Location of Two Points on Either Side of the Crack Where Displacement is Measured by Speckle Interferometry

The computations were made using plane stress assumptions. Plane stress calculations were chosen based on the analysis reported by Atluri and Nakagaki [10] where theoretical plane stress J-integral values gave the best agreement with 1.0 inch thick compact type specimen test data. The thickness of the compact type specimens used in the present work is 0.5 inches. Plane stress computations were also chosen by Hinnerichs et al [4] to analyze creep crack

growth in a centre-cracked plate which had a thickness of 0.3 inches with crack lengths as small as 0.12 inches.

Figure 4 shows the finite element mesh used to analyze one half of the compact type specimen. The mesh for the creep crack growth computations consists of 115 isoparametric 8 noded quadrilateral elements with 420 node points. Reduced integration was employed in the analysis so that the surface integrations over each element, required in the formulation of the matrices in equation (3), employed only four Gaussian integration points per element. Thirty six square elements, each of dimension 0.01 inches by 0.01 inches, are located in the area immediately surrounding the crack tip. Details of the crack tip mesh are displayed in Figure 5.

The adequacy of the mesh was checked by computing the elastic stress intensity factor generated by the finite element model under plane strain conditions. Agreement with the handbook formula [11] for the elastic stress intensity factor was achieved to within 3% accuracy.

Initially, the continuum damage model was incorporated into the unified viscoplastic constitutive formulation, and the complete constitutive/continuum damage model was coded into a FORTRAN subroutine of the ABAQUS finite element program. When the compact type specimen is initially loaded to 4000 lbs., a rapid stress redistribution occurs at the Gaussian integration points closest to the crack tip. The stress at the point closest to the crack tip relaxes (decreases) while the stresses at the points further removed from the crack tip increase slightly to preserve global equilibrium. After about 10 seconds the stress redistribution stabilizes and no further change in the state of the compact type specimen occurs until about 94 minutes have elapsed. The equivalent Von Mises stress at the Gaussian integration point closest to the crack tip, viz., point 2 in element number 83 of Figure 6, has a value of 139200 lb/in^2. The equivalent stress at integration point 1 of element 83 which is further removed from the crack tip has a much lower value of 100600 lb/in^2. After 94 minutes at the constant stabilized stress value of 139200 lb/in^2, integration point 2 in element 83 begins to rapidly accumulate creep damage and failure (creep rupture) occurs after 94.2 minutes. At this point the integration procedure becomes unstable as the damage parameter approaches values close to unity.

The constitutive equations, when written in differential form, will always tend to exhibit unstable behaviour whether or not explicit forward difference or implicit backward difference methods are used in the integration procedure. The tendency to unstable behaviour in the differential equations arises from the fact that the right hand sides of the differential equations become very large as the damage parameter approaches unity. An integral formulation of the viscoplastic model is given in Appendix 1, where it may be seen that the factor (1-D) appears on the right hand side of the equation for the stress. As D approaches unity the stress decreases to zero

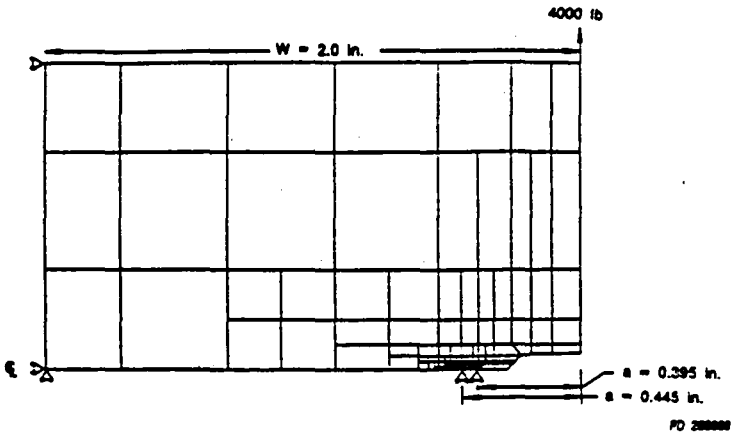

Figure 4. - Finite Element Mesh for Creep Crack Growth in Compact Type Specimen

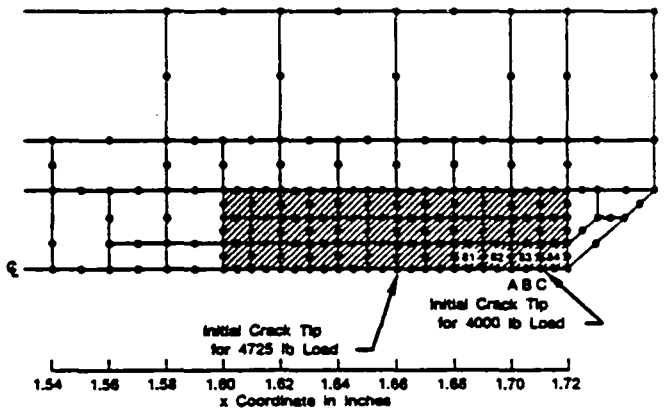

Figure 5. - Detail of Crack Tip Region in Compact Type Specimen

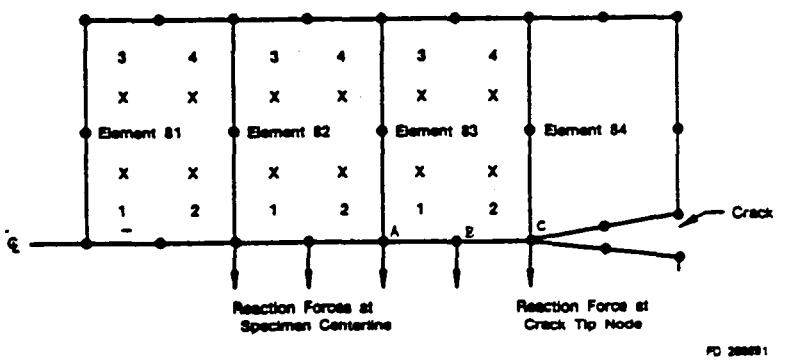

Figure 6. - Detail of Crack Tip Showing Reaction Forces and Gaussian Integration Points

and no instability should be encountered if an integral recursion procedure is used to step from the beginning to the end of the increment. This procedure was not used in the present calculations because a suitable algebraic Jacobian matrix was only developed after the present calculations were completed. Recent applications of the numerical procedure using the integral recursion relations have proved successful, and this method ought to be pursued further in an attempt to obtain a stable integration method for the coupled viscoplastic/damage equations.

Since the equivalent stress at the integration point closest to the crack tip remains constant for 94 minutes after the initial 10 to 15 second transient, and failure occurs at 94.2 minutes, it was decided to remove the damage computation from the viscoplastic FORTRAN subroutine to avoid the instability due to creep continuum damage accumulation.

The computations for creep crack growth now proceed as follows. First, the compact type specimen is loaded to either 4000 lbs. or to 4725 lbs. After a brief transient stress redistribution in the vicinity of the crack tip, the equivalent stress remains constant at the Gaussian integration point closest to the crack tip, viz. integration point 2 in element 83 of Figure 6. The time to failure for this integration point can then be determined from equation (2). From equation (5) of Appendix 3, the last two terms are responsible for decreasing the stress at the material point due to the growth of the creep damage parameter D. That is to say, as the point fails and its load carrying capacity diminishes with increasing damage, the stress at that point decreases and the load which it carries is shed onto other surrounding material points in the structure. To simulate this decrease in the load carrying capacity of the Gaussian integration point, four load increments are carried out in which the stress components are reduced by one half of their value at the beginning of each increment. Each increment lasts for 0.25 seconds, so that once failure is deemed to have occurred, the stress is reduced to about 6% of its initial stabilized value at the integration point in 1 second. In each succeeding increment the stress is further reduced by one half of its value as the analysis proceeds. Integration point 2 of element 83 in Figure 6 has now failed. The displacement boundary conditions at crack tip node C in Figure 6 are replaced by force boundary conditions. The reaction force required to hold the crack tip node C in its current location is then released in four (4) increments over a period of 1 second and the crack advances to the adjacent node B halfway through the isoparametric element.

A brief transient stress redistribution lasting for about 15 seconds again occurs, followed by a stabilized condition. The equivalent stress after stabilization is then computed at integration point 1 of element 83, and the time to rupture determined once again from equation (2). Once failure has occurred the stress is shed from integration point 1 to about 6% of its initial value in 1 second, and the crack tip node B is released in four increments over a

1 second period and the crack advances completely through the isoparametric element to the adjacent node A. This procedure is repeated for all nodes lying in the crack plane ahead of the advancing crack.

The justification for the decoupling of the viscoplastic and continuum damage constitutive models is based on the following observations:

(1). The stress falls off very rapidly in the crack plane of a compact type specimen. Consequently the stress at the integration point closest to the crack tip is large and the rupture or failure time is fairly small. The second integration point in the crack tip element and the integration points further away are subjected to such small stresses that the amount of creep damage accumulated by these points, at the time the integration point closest to the crack tip fails, is practically zero. The creep rupture time in equation (2) can then be used for each integration point in turn. Even if the damage accrued by each point is not small, the rupture time can still be determined from equation (1) by integration.

(2). The transient stress distribution after initial load up or after a node release, redistributes in a time which is much smaller than the time required to fail or rupture the integration points closest to the crack tip. Each integration point is therefore subjected to a constant stabilized stress for most of its life.

These observations are pertinent to high strength superalloy materials and are not expected to hold true for ductile materials of lower strength.

EXPERIMENTAL MEASUREMENTS

The standard compact type specimen shown in Figure 7 was used to obtain the creep crack growth rate data. Testing was conducted on a hydraulic constant load test frame. All precracking and testing was performed in accordance with the procedures outlined in ASTM 647-83. Specimen heating was provided by resistance, clamshell furnaces having windows to allow observation of the crack growth at test temperatures. The crack extension under creep loading conditions was determined by a laser heterodyne optical strain measurment system using speckle interferometry.

The concept of the heterodyne optical strain measurement system is illustrated in Figure 8. A laser beam is split into two parallel beams illuminating two closely spaced points on the object. The comparatively rough surface of the object scatters the laser light in a random manner resulting in two speckle fields reflected from the surface of the object. These two speckle fields are imaged by a lens system onto the film plane. If a photographic plate is placed at the film plane, a photographic recording of the resulting speckle interference pattern is made.

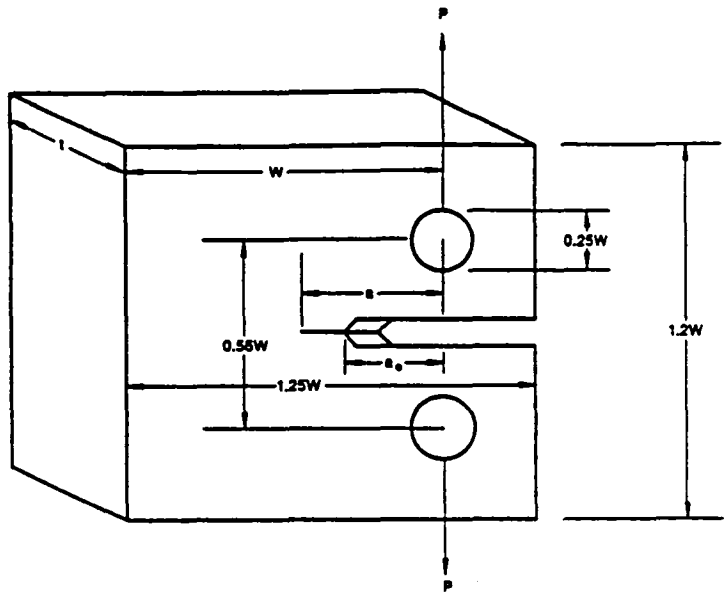

Creep Specimens	
P =4000 W =2.0 a_o = 0.275 a = 0.395 t = 0.5	P =4725 W =2.0 a_o = 0.275 a = 0.445 t = 0.5

Fatigue Specimen
P_{max} = 3089, P_{min} = 307 W = 2.5 a_o = 0.375 a = 0.505 t = 0.5

FD 268892

Figure 7. - Dimensions of Compact Type Specimens Used in Creep and Fatigue Crack Growth Experiments

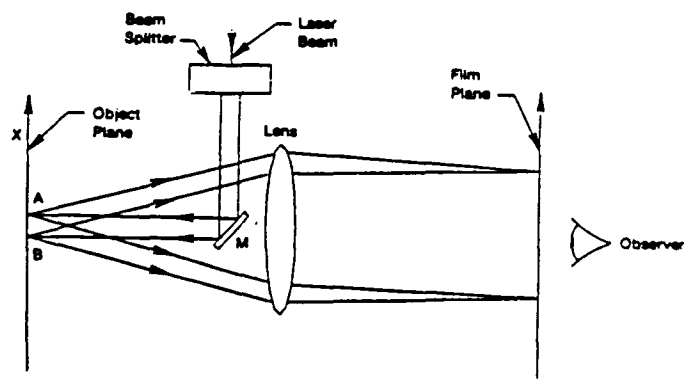

FD 268894

Figure 8. - Optical Strain Measurement Concept

The recording of the speckle interference pattern is then relocated in the same position it occupied during exposure. When the object is loaded in the X direction (Figure 8) causing points A and B on the object to separate in-plane, the spatial frequency of the fine interference fringes will change relative to the pattern previously recorded on the photographic plate with no load on the object. The effect of this change in frequency is to generate a change of phase angle between the interference pattern reflected from the object and the one recorded on the plate. The result to the observer will be the creation of a Moiré fringe pattern, each fringe of which represents a 180 degree shift in phase. The spatial frequency of these Moiré fringes is proportional to the strain on the object between points A and B.

In previous methods, the Moiré fringes were simply counted and the number of fringes directly related to strain. However, these methods have significant limitations in accurately measuring strain. For example, strain values corresponding to less than one fringe across the field of view cannot be measured; location of the fringe centres is not accurate; and no distinction is made between positive and negative strain. All of these undesirable limitations can be eliminated by the incorporation of heterodyned interferometry.

To implement heterodyned interferometry into the system shown in Figure 8, a device for constantly changing the phase of the laser beam prior to the beam splitter is added. This causes the Moiré fringes observed on the film plame to scan across the field of view in a constant direction. If the observer is replaced by a photodiode, the output of which is supplied to a phase meter, small changes in phase can easily be measured. Phase meters can accurately measure phase changes to within 0.5 degree, which is equivalent to dividing each Moiré fringe into 1000 parts. Therefore, heterodyned readout of the Moiré fringe pattern greatly increases the resolution and accuracy over typical optical techniques.

The heterodyne optical strain measurement system developed in the Materials Engineering and Technology Laboratory of Pratt & Whitney Aircraft is shown in Figure 9. A 2 watt argon ion laser is used and the heterodyne signal is provided by a $\lambda/2$ retarder plate mounted in the hollow shaft of an electric motor and by a stationary $\lambda/4$ retarder. The laser beam is split by a calcite beam displacer into two parallel beams 0.1 inches apart, which are then directed by mirrors to the specimen. Light scattered from the specimen is gathered by the strain sensor head and focused onto the photographic plate located in the plate holder. Two photodiodes are placed directly behind the plate.

The signals from the photodiodes, after being amplified and filtered, are fed into a counter that measures the phase of the signal from one of the diodes relative to the other. To conduct elevated temperature tests, an enclosure to stagnate the air between the specimen and the photodiodes is required as shown in Figure 9. An access port in the side of the furnace allows the light to reach the specimen and reflect back to the sensor head through a tunnel. The box around the sensor head helps stagnate the air and also shields the photodiodes from room lights.

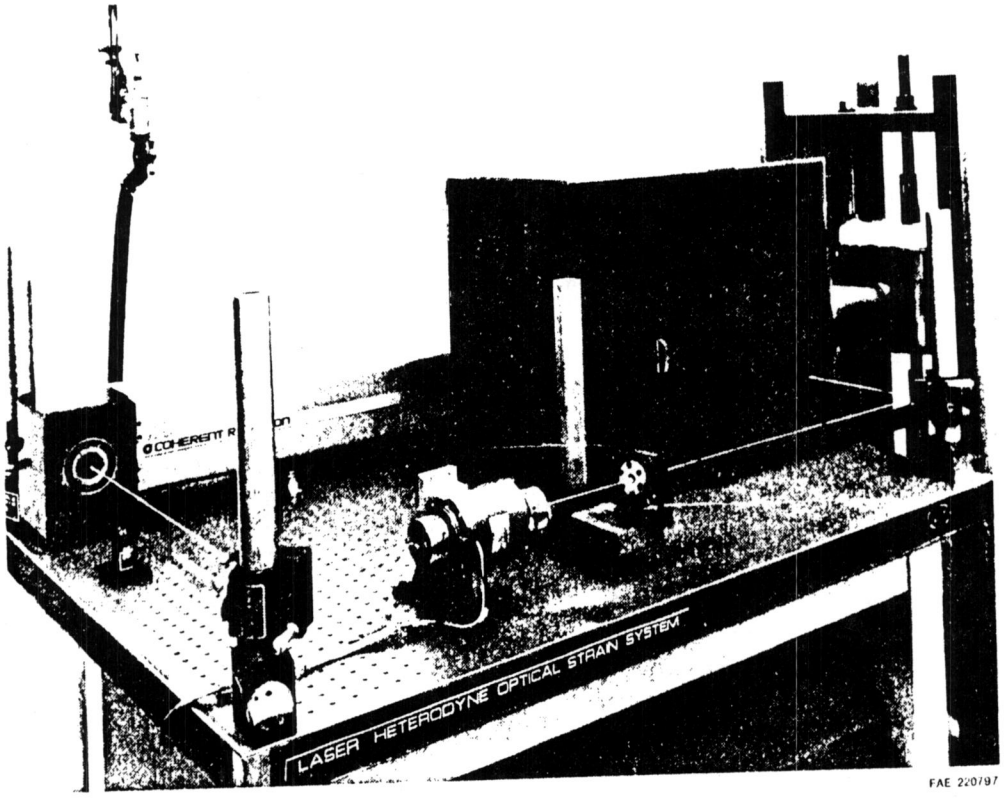

Figure 9. - Optical Strain System With Furnace, Tunnel, and Enclosure In-Place

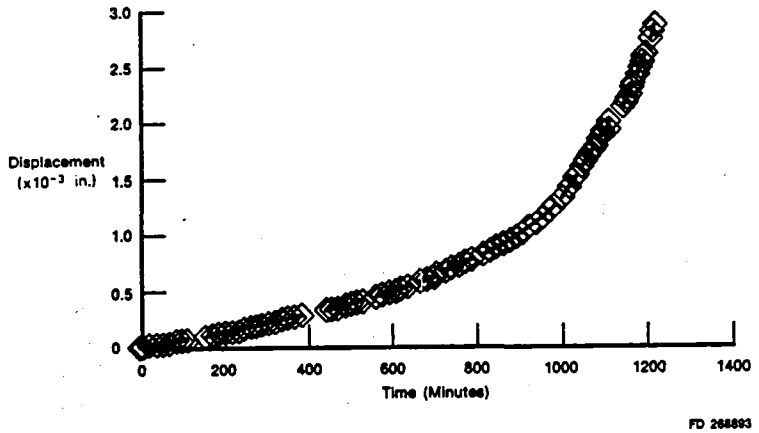

Figure 10. - Displacement from Centerline in the y-direction of Speckle Interferometry Point for Specimen Load of 4000 lbs

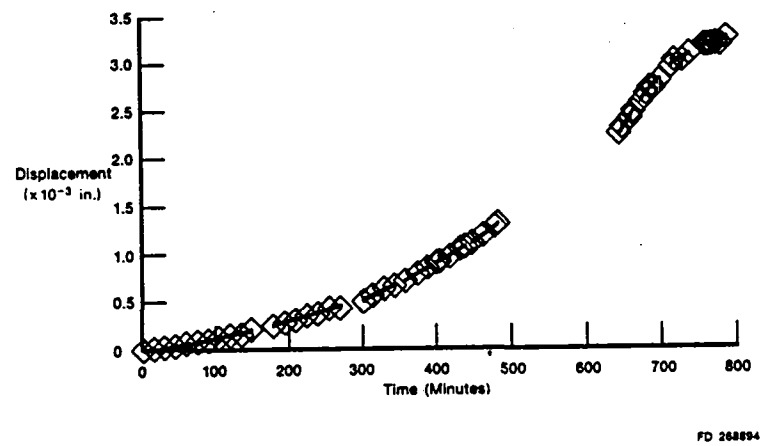

Figure 11. - Displacement from Centerline in y-direction of Speckle Interferometry Point for Specimen Load of 4725 lbs

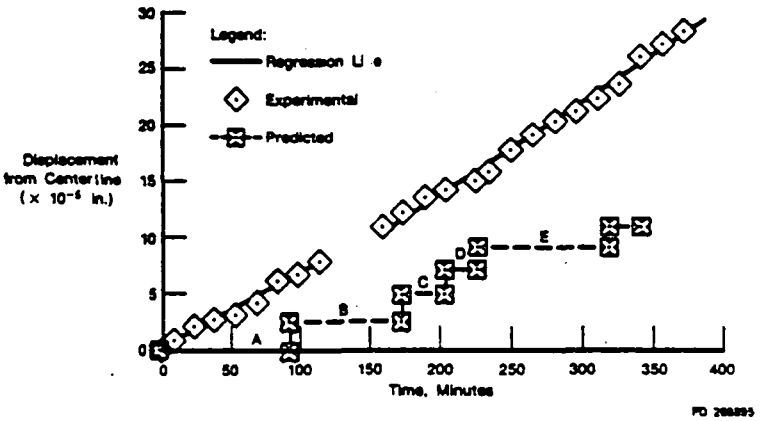

Figure 12. - Comparison of Measure and Predicted Displacements for Loads of 4000 lbs

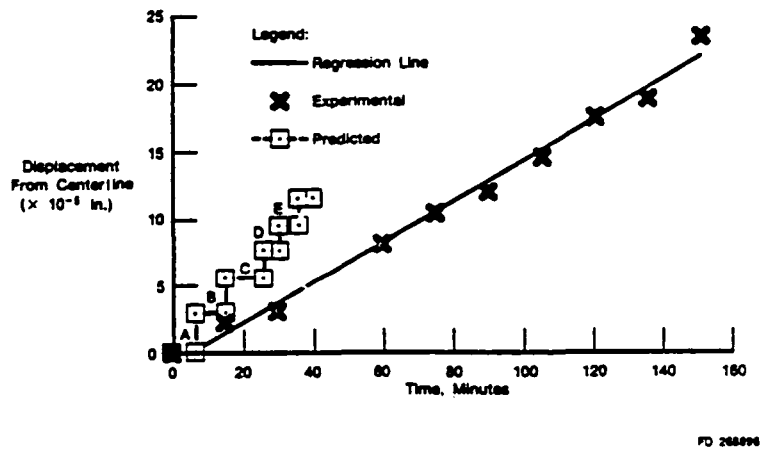

Figure 13. - Comparison of Measured and Predicted Displacements for Loads of 4725 lbs

RESULTS

The displacement of two points, located on either side of the crack tip, as shown in Figure 3, was measured as a function of time by the speckle interferometry technique described in the preceding section. Figures 10 and 11 show the experimental displacement of one of the points in the y direction (see Figure 3) as a function of time elapsed after application of load to the compact type specimen. The displacement is measured with respect to the centreline of the specimen and represents an average value for the two locations.

Theoretical and experimental results corresponding to the initial portions of these curves are displayed in Figures 12 and 13. The portions of the curves labelled A,B,C,D,E in these figures correspond to the stabilized behaviour of the compact type specimen after the 15 second transient and prior to the release of the 1st, 2nd, 3rd, 4th and 5th nodes ahead of the crack tip. The material constants A and r in the creep rupture equation (2) are chosen to give a least square fit to the uniaxial creep rupture data generated in the present work, as opposed to the values quoted in Figure 2, which correspond to a least square fit to three sets of independent data.

It is clear from Figures 12 and 13 that the computed displacement, and hence the computed initial creep crack growth rate, is too small by about a factor of two at the 4000 lb. loading level, and too large by a factor of two at the 4725 lb. loading level. Hence, the material constants generated from the uniaxial creep rupture data also give an approximate least square fit to the creep crack growth data.

Agreement between the predicted and experimental creep crack growth rates can easily be achieved simply by doubling and halving the computed creep rupture times (required to fail the Gauss points ahead of the crack tip) for the 4725 lb. and 4000 lb. load cases. A logarithmic plot of equivalent Von Mises stress at the Gauss points versus rupture time, which gives agreement between the experimental and finite element displacements at the speckle interferometry points, is given in Figure 2. As expected, the points lie on either side of the least square data line obtained from the three sets of uniaxial creep rupture data.

CONCLUDING REMARKS

Creep crack growth has been measured in compact type specimens of INCO 718 at 1200°F (649°C). Theoretical predictions of crack growth were made by employing the ABAQUS nonlinear general purpose finite element program in conjunction with a unified viscoplastic constitutive model and a continuum damage failure criterion.

The results of the current work may be summarized as follows:

(1). Initial creep crack growth rates at 1200°F (649°C) in the INCO 718 compact type specimens can be predicted by the theoretical model.

Crack growth is assumed to take place due to creep rupture of the material in the immediate vicinity of the crack tip and material constants for the continuum damage creep failure model were determined from creep rupture tests on uniaxial bar specimens of INCO 718 at 1200°F (649°C). Calculations were performed under plane stress conditions.

(2). The differential form of the unified viscoplastic constitutive model becomes very unstable when continuum damage is included in the formulation. It appears that the integral formulation of the unified viscoplastic model given in Appendix 1 should be used to obtain a stable integration algorithm.

(3). Speckle interferometry appears well suited for high temperature creep crack growth measurement.

REFERENCES

1. K.P. Walker and D.A. Wilson, "Constitutive Modeling of Engine Materials", Draft of Final Report FR-17911 to AFML Contract F33615-81-C-5040.

2. Users' Manual, Example Problems Manual, Systems Manual and Theory Manual for the ABAQUS general purpose nonlinear finite element program developed by Hibbitt, Karlsson & Sorensen, Inc. 35 South Angell St., Providence, R.I., 02906.

3. A.S. Kobayashi, "Current and Future Experimental Methods", Fracture Mechanics, Edited by N. Perrone, H. Liebowitz, D. Mulville and W. Pilkey, 10th Symposium on Naval Structural Mechanics, Washington, D.C., 1978.

4. T.D. Hinnerichs, "Viscoplastic and Creep Crack Growth Analysis by the Finite Element Method", Report AFWAL-TR-80-4140, Wright-Patterson Air Force Base, Ohio, 1981.

5. W.N. Sharpe, Jr., Unpublished Data on USAF Contract F33615-77-C-5003, Wright-Patterson Air Force Base, Ohio, 1979, (cf. Reference 4.).

6. P.A. Domas, W.N. Sharpe, M. Ward and J. Yau, "Benchmark Notch Test for Life Preditions", Final Report NASA CR-165571 on NASA Lewis Contract NAS3-22522, 1982.

7. K.P. Walker, "Research and Development Program for Nonlinear Structural Modeling with Advanced Time-Temperature Dependent Constitutive Relationships", Final Report NASA CR-165533 on NASA Lewis Contract NAS3-22055, 1981.

8. J.L. Chaboche, "Thermodynamic and Phenomenological Description of Cyclic Viscoplasticity with Damage", Translation of Publication No. 1978-3 of the Office National d'Etudes et de Researches Aerospatiales, France, by the European Space Agency Technical Translation Service, Publication No. ESA-TT-548, 1979.

9. A.B. Thakker and B.A. Cowles, "Low Strain, Long Life Creep Fatigue of AF2-1DA and INCO 718", Final Report NASA CR-167989 on NASA Lewis Contract NAS3-22387, 1983.

10. S.N. Atluri and M. Nakagaki, AIAA Journal, Vol 15, No. 7, pp. 923-931, 1977.

11. ASTM E647-83, Section 9.3.1.

Appendix 1

COUPLED CONTINUUM DAMAGE/INTEGRAL VISCOPLASTIC FORMULATION

$$\sigma_{ij}(t) = \frac{2}{3}\Omega_{ij}(t) + (\lambda(t) + \frac{2}{3}\mu(t))(1 - D(t))\,\delta_{ij}\epsilon_{kk} + \int_0^t e^{-\{Q(t) - Q(\xi)\}} \Big\{ 2\mu(\xi)(1 - D(\xi))\frac{\partial \epsilon_{ij}}{\partial \xi} - \frac{2}{3}\mu(\xi)(1 - D(\xi))\delta_{ij}\frac{\partial \epsilon_{kk}}{\partial \xi} - \frac{2}{3}\frac{\partial \Omega_{ij}}{\partial \xi} + \frac{1}{\mu(\xi)}\frac{\partial \mu}{\partial \xi}\frac{2}{3}\Omega_{ij}(\xi) \Big\} d\xi \,, \tag{1}$$

$$\Omega_{ij}(t) = \dot{\Omega}_{ij}(t) + n_1(t)c_{ij}(t) + n_2(t)\int_0^t e^{-\{G(t) - G(\xi)\}}\frac{\partial c_{ij}}{\partial \xi}\,d\xi \,, \tag{2}$$

$$K(t) = K_1(t) - K_2(t)e^{-n_7(t)R(t)} \,, \tag{3}$$

$$c_{ij}(t) = \epsilon_{ij}(t) + \frac{\lambda(t)}{2\mu(t)}\delta_{ij}\epsilon_{kk}(t) - \frac{\sigma_{ij}(t)}{2\mu(t)(1 - D(t))} \,, \tag{4}$$

$$\dot{\Omega}_{ij}(t) = -\delta_{ij}\dot{\Omega}(t) + 3\dot{\Omega}(t)\frac{c_{ik}(t)c_{kj}(t)}{c_{pq}(t)c_{pq}(t)} \,, \tag{5}$$

$$Q(t) = \int_0^t \left\{ \frac{3\mu(\xi)}{K(\xi)} \frac{1}{\log(1 + \beta\frac{\partial R}{\partial \xi})} \frac{\partial R}{\partial \xi} - \frac{1}{\mu(\xi)}\frac{\partial \mu}{\partial \xi} \right\} d\xi \,, \tag{6}$$

$$G(t) = \int_0^t (n_3(\xi) + n_4(\xi)e^{-n_5(\xi)R(\xi)})\frac{\partial R}{\partial \xi}\,d\xi \,, \tag{7}$$

$$R(t) = \int_0^t \sqrt{\frac{2}{3}\frac{\partial c_{ij}}{\partial \xi}\frac{\partial c_{ij}}{\partial \xi}}\,d\xi \,. \tag{8}$$

Appendix 2

CHABOCHE'S CREEP DAMAGE MODEL

$$\dot{D} = A \left\langle \frac{\sqrt{3/2\, S_{ij}\, S_{ij}}}{1-D} \right\rangle^{r} (1-D)^{r-k}, \tag{1}$$

$$k = 1 + (1.011 \times 10^{-4}) \exp\left(9.446 \times 10^{-5} \sqrt{3/2\, S_{ij}\, S_{ij}}\right) \tag{2}$$

The constants are chosen to have the values:

$A = 2.394 \times 10^{-43}$, $r = 7.22$.

Appendix 3

UNIFIED VISCOPLASTIC EXPONENTIAL LAW FOR UNIFIED FORMULATION

$$\dot{\epsilon}_{ij} = \frac{\exp\left(\frac{\sqrt{2/3(3\alpha_{ij}/2 - \Omega_{ij})(3\alpha_{ij}/2 - \Omega_{ij})}}{K(1-D)}\right) - 1}{\beta} \frac{(3\alpha_{ij}/2 - \Omega_{ij})}{\sqrt{2/3(3\alpha_{ij}/2 - \Omega_{ij})(3\alpha_{ij}/2 - \Omega_{ij})}}, \tag{1}$$

$$\dot{\Omega}_{ij} = n_2\, \dot{\epsilon}_{ij} - \dot{G}_1\, \Omega_{ij}, \tag{2}$$

$$\dot{G}_1 = (n_3 + n_4\, e^{-n_5 R})\, \dot{R}, \tag{3}$$

$$K = K_1 + K_2\, e^{-n_7 R}, \tag{4}$$

$$\dot{\sigma}_{ij} = \delta_{ij}\lambda(1-D)\dot{\epsilon}_{kk} + 2\mu(1-D)\,(\dot{\epsilon}_{ij} - \dot{\epsilon}_{ij}) + \delta_{ij}\,\dot{\lambda(1-D)}\,\epsilon_{kk} + \dot{2\mu(1-D)}\,(\epsilon_{ij} - c_{ij}), \tag{5}$$

$$\dot{R} = \sqrt{2/3\dot{\epsilon}_{ij}\dot{\epsilon}_{ij}} \tag{6}$$

$$s_{ij} = \sigma_{ij} - \frac{1}{3}\,\delta_{ij}\sigma_{kk}. \tag{7}$$

The constants are chosen to have the values:

$\lambda = 1.517$ E7, $\mu = 1.012$ E7, $K_1 = 4219$, $K_2 = -1438$, $\beta = 6.203$ E9, $n_2 = 22.4$ E6,
$n_3 = 269.6$, $n_4 = 0$, $n_5 = 0$, $n_7 = 14$.

For no cyclic softening $K_1 = 5657$ and $K_2 =$

☆U.S. GOVERNMENT PRINTING OFFICE:1985-537-086/ 20003 REGION NO. 4